Chemical Science

ROYAL SOCIETY OF CHEMISTRY

EDGE ARTICLE

View Article Online
View Journal | View Issue

Cite this: *Chem. Sci.*, 2022, **13**, 3477

All publication charges for this article have been paid for by the Royal Society of Chemistry

A reactivity model for oxidative addition to palladium enables quantitative predictions for catalytic cross-coupling reactions†

Jingru Lu, Sofia Donnecke, Irina Paci * and David C. Leitch *

Received 11th January 2022
Accepted 28th February 2022

DOI: 10.1039/d2sc00174h

rsc.li/chemical-science

Making accurate, quantitative predictions of chemical reactivity based on molecular structure is an unsolved problem in chemical synthesis, particularly for complex molecules. We report an approach to reactivity prediction for catalytic reactions based on quantitative structure-reactivity models for a key step common to many catalytic mechanisms. We demonstrate this approach with a mechanistically based model for the oxidative addition of (hetero)aryl electrophiles to palladium(0), which is a key step in myriad catalytic processes. This model links simple molecular descriptors to relative rates of oxidative addition for 79 substrates, including chloride, bromide and triflate leaving groups. Because oxidative addition often controls the rate and/or selectivity of palladium-catalyzed reactions, this model can be used to make quantitative predictions about catalytic reaction outcomes. Demonstrated applications include a multivariate linear model for the initial rate of Sonogashira coupling reactions, and successful site-selectivity predictions for Suzuki, Buchwald-Hartwig, and Stille reactions of multihalogenated substrates relevant to the synthesis of pharmaceuticals and natural products.

Introduction

The synthesis of structurally complex organic molecules relies on forging new chemical bonds between diverse molecular building blocks. Catalytic cross-coupling is one of the most versatile and widely-used methods to link these molecular fragments,[1] with applications ranging from the manufacture of active pharmaceutical ingredients,[2] to the selective modification of biomolecules,[3] to the creation of new functional materials.[4] While much has been done to develop and understand new cross-coupling reactions and catalysts, less is known about how the specific molecular structures of complex building blocks affect the likelihood of successful coupling.[5–7] As a result, time- and resource–intensive reaction screening and optimization campaigns are often required for each new synthetic target. These involve many iterations and can still result in failure to find appropriate conditions for a given transformation, impeding access to potentially promising new medicines and materials.

Emerging approaches in reactivity prediction that combine high-throughput experimentation[8–14] with molecular descriptor sets[15–24] and multivariate statistical analysis including machine learning[25–34] can accelerate the screening/optimization process and increase success rates; however, predictions generated by these approaches are often limited to the specific reaction under investigation. Developing and refining the next generation of organic chemistry tools, including computer-aided synthesis design, automated reaction optimization, and predictive algorithms,[35] requires the development of general and quantitative frameworks that rapidly link molecular structure to reactivity for many different reactants and catalysts.

Here, we describe an approach to predict outcomes for multiple catalytic cross-coupling reactions by focusing on the structure–reactivity relationships for one key mechanistic step (Fig. 1). Specifically, we targeted oxidative addition, a fundamental organometallic transformation common to many catalytic reactions.[36] Oxidative addition is particularly relevant to palladium-catalyzed cross-coupling, where it is often the rate and/or selectivity determining step[37] (Fig. 1A). We hypothesized that a quantitative structure-reactivity model for the oxidative addition[38–40] of aryl electrophiles to a catalytically-relevant Pd(0) complex would enable predictions for palladium-catalyzed cross-coupling reactions under a variety of conditions. We assembled this model by correlating experimental relative rate data (Fig. 1B) with easily-obtained molecular descriptors for a diverse set of substrates, with an emphasis on incorporating pharmaceutically-relevant heterocycles (Fig. 1C).

As hypothesized, the resulting model can be applied to many different cross-coupling reactions. It can predict catalytic rate constants as a function of substrate structure even when different catalysts/solvents are used, can correctly identify the

Department of Chemistry, University of Victoria, 3800 Finnerty Rd, Victoria BC, V8P 5C2, Canada. E-mail: ipaci@uvic.ca; dcleitch@uvic.ca

† Electronic supplementary information (ESI) available: Detailed experimental and computational procedures, statistical modeling information, supplementary figures, tables of molecular descriptors, and coordinate files for calculated structures. See DOI: 10.1039/d2sc00174h

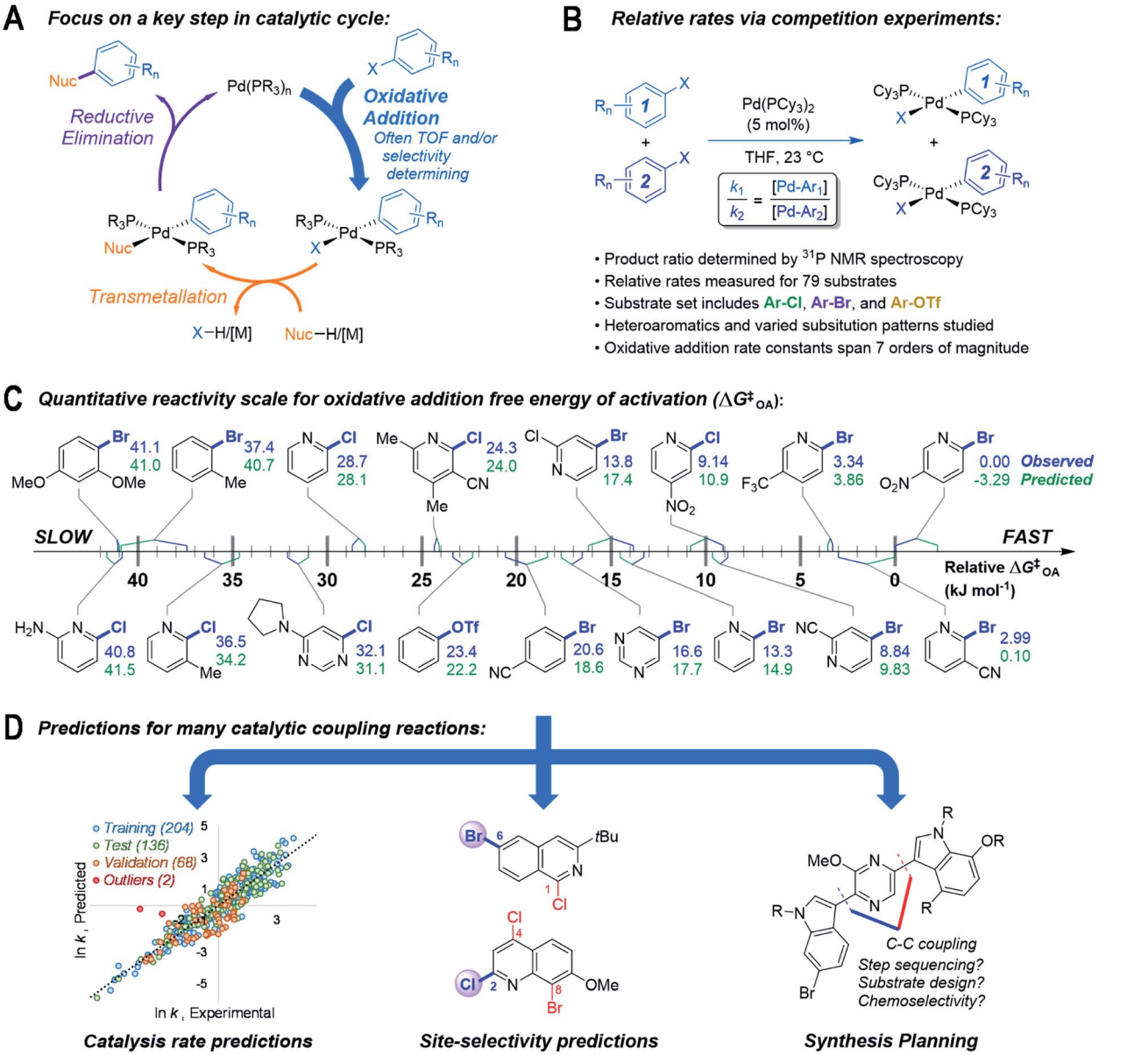

Fig. 1 (A) Simplified cross-coupling mechanism, highlighting oxidative addition as the rate and/or selectivity determining step. (B) Competition experiment approach to determining relative rates of oxidative addition by quantifying ratios of Pd(II) products *via* ^{31}P NMR spectroscopy. (C) Relative reactivity scale for oxidative addition to $Pd(PCy_3)_2$ for selected substrates; observed $\Delta G^{\ddagger}_{OA}$ for 2-bromo-5-nitropyridine set to 0 kJ mol^{-1}. (D) Utility of reactivity model in predictions for cross-coupling in synthesis.

most reactive position(s) when multiple reaction sites are available, and can also help to guide synthetic route planning (Fig. 1D). Importantly from both a fundamental and practical perspective, the predictive ability of this reactivity model extends well beyond the specific molecular structures and reaction conditions included in the initial data set. By revealing how subtle changes to the reacting molecules affect a key step in a catalytic mechanism, this model serves as a powerful predictive tool for cross-coupling, and will enable more sophisticated and accurate computer-aided retrosynthetic design. Finally, this work demonstrates the potential of focusing reaction prediction efforts on fundamental mechanistic steps in catalytic mechanisms.[41]

Results and discussion

Development of the oxidative addition reactivity model

As the basis for a quantitative structure/reactivity model for cross-coupling catalysis, we conducted a series of oxidative addition competition experiments in THF using a library of 79 (hetero)aryl chlorides, bromides, and triflates, reacting with $Pd(PCy_3)_2$ (Fig. 1B). Measuring the Pd(II) product ratio by ^{31}P NMR spectroscopy gives relative observed rate constants, and the corresponding relative free energies of activation ($\Delta G^{\ddagger}_{OA}$), with 2-bromo-5-nitropyridine set to $\Delta G^{\ddagger}_{OA} = 0$.

As a check on these kinetic data, we constructed Hammett plots for five sets of substrates, obtaining reaction constants

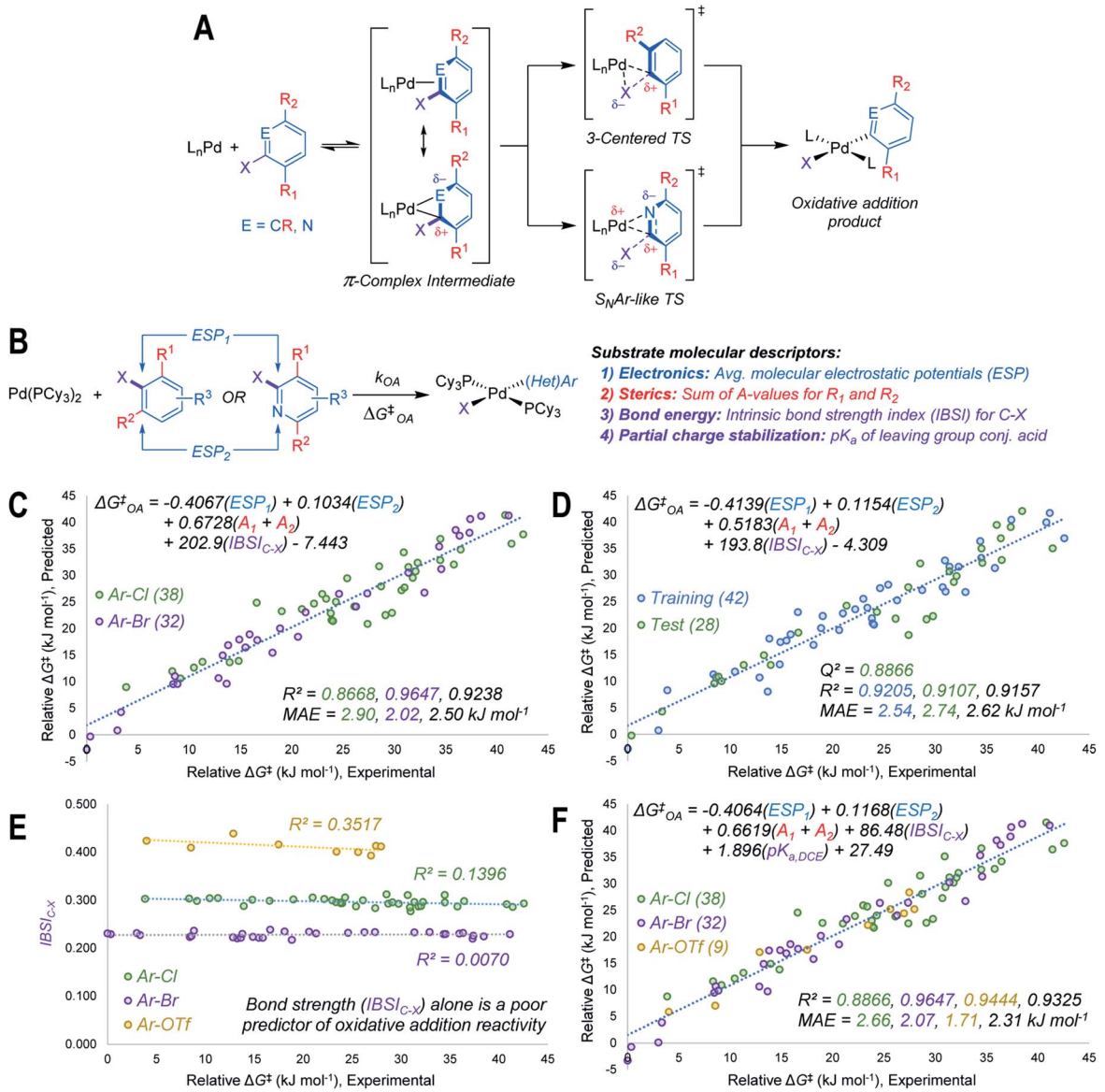

Fig. 2 Design and performance of a quantitative reactivity model for oxidative addition to Pd(0). (A) General mechanism for oxidative addition to $L_nPd(0)$, with π-complex intermediate preceding either Pd insertion into C–X bond, or an S_NAr-like displacement of X. (B) Molecular descriptors used to model oxidative addition reactivity as a function of substrate structure. (C) Multivariate linear regression model of $\Delta G^{\ddagger}_{OA}$ for 70 Ar–Cl and Ar–Br substrates in THF, including all data points in regression analysis. (D) Representative multivariate linear regression model generated using a 60/40 training/test split. (E) Univariate plot of $IBSI_{C-X}$ *versus* $\Delta G^{\ddagger}_{OA}$ for Ar–Cl, Ar–Br, and Ar–OTf, revealing that bond strength is poorly correlated to $\Delta G^{\ddagger}_{OA}$ within each leaving group set. (F) Unified linear regression model of $\Delta G^{\ddagger}_{OA}$ for Ar–Cl, Ar–Br, and Ar–OTf substrates in THF, including all data points in regression analysis. MAE = mean absolute error. Colour-coding on R^2, Q^2, and MAE values corresponds to the matching data subset, values in black are for all data.

consistent with previous reports (Fig. S31–S37†). From these data, we have constructed a unified reactivity scale that spans more than 7 orders of magnitude in rate (Fig. 1D), containing substrates with a wide variety of steric and electronic parameters, as well as the three aforementioned leaving groups. We also ruled out the possibility of reversible oxidative addition leading to thermodynamic product ratios by mixing equimolar amounts of six separate pairs of oxidative addition products, all of which retained their 1 : 1 mole ratio even after extended time (Table S3†). Finally, we isolated and characterized six new representative Pd(II) oxidative addition complexes to confirm their structures as *trans*-$Pd(PCy_3)_2(Ar)(X)$ (compounds S1–S6, Fig. S7–S30†).

Using the mechanistic features of oxidative addition to Pd(0) as a guide, we considered molecular descriptors that would provide mechanistically meaningful correlations between substrate structures and oxidative addition reactivity (Fig. 2A).[39] Mechanisms for aryl halide oxidative addition to Pd(0) have been extensively studied both computationally[40,42–44] and experimentally,[45–49] and are generally proposed to proceed *via*

Table 1 Identified outliers in oxidative addition regression model for Cl, Br, and OTf substrates (Fig. 2F)

$\Delta G^{\ddagger}_{OA}$ (kJ mol^{-1})	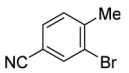	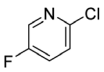	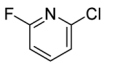	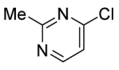
Observed	32.92	29.76	29.12	16.57
Predicted	26.74	23.29	22.67	24.59
Residual	6.18	6.37	6.45	−8.02

initial coordination of the aromatic π-system to Pd. Two bonding extremes can be envisioned for the π-complex intermediate, where the degree of polarization of the coordinated C=C or C=N bond in the substrate influences partial charge distribution in the π-complex. From this intermediate, two types of oxidative addition transition state have been proposed: a 3-centered, relatively non-polar transition state involving simultaneous Pd–C and Pd–X bond formation, and a polarized transition state with C–X heterolytic bond cleavage occurring alongside Pd–C bond formation; this latter pathway resembles the proposed mechanism for nucleophilic aromatic substitution (S_NAr).[46,49] While other coordination modes between the (hetero)aryl substrate and Pd are possible, we restricted our analysis to the π-complex intermediates that would immediately precede oxidative addition.

Based on the structural and electronic features of these transition states, we built our reactivity model for oxidative addition from a combination of average molecular electrostatic potentials (ESP) as electronic descriptors for specific atoms in the substrate,[38,50–54] A-values as steric descriptors,[55] and the intrinsic bond strength index (IBSI) as a bond energy descriptor (Fig. 2B).[56] Importantly, all of these descriptors are directly calculated from electronic wavefunctions (obtained from density functional theory calculations), or are tabulated in the literature. An initial multivariate linear regression analysis[27,57] of the descriptor sets for the Ar–Cl and Ar–Br substrates *versus* relative $\Delta G^{\ddagger}_{OA}$ (kJ mol^{-1}) reveals a strong correlation across the halide substrate library (Fig. 2C).

This model incorporates two ESP values: one for the carbon undergoing substitution (ESP_1), and a second for an atom adjacent to the reactive site (ESP_2). For 2-halopyridines, ESP_2 corresponds to the nitrogen atom. For substrates where the adjacent atoms are inequivalent carbons, which would lead to two possible π-coordination sites prior to oxidative addition, ESP_2 is the value that leads to the smaller predicted $\Delta G^{\ddagger}_{OA}$ (*i.e.* the faster oxidative addition); either the smaller positive value, or the larger negative value. The model also incorporates two substituent *A*-values for groups R_1 and R_2 to account for steric effects on the oxidative addition rate. While the steric effect of groups *ortho* to the reactive C–X bond is intuitive, the effect of R_2 for 2-halopyridine substrates is not initially obvious; however, our experimental results reveal the steric influence of R_2 is approximately equal to that of R_1 throughout the 2-halopyridine substrate set. As these two terms have very similar coefficients when treated separately during linear regression (Table S8†), we opted to use the sum (A_1 + A_2) as a single descriptor. Finally, including the IBSI is necessary to create a model applicable to both (hetero)aryl chlorides and bromides.

We evaluated the robustness of this linear model by regression analysis of five random training (60%) and test (40%) sets, and comparing the mean absolute errors (MAE) and predictive squared correlation coefficients (Q^2);[58] one example is shown in Fig. 2D (remainder in Fig. S60–S63†). All of these analyses give similar linear equations, and excellent agreement between predicted and experimental values in the test sets. We also evaluated alternative models (Table S9†), and partitioned the data into targeted training and test sets to evaluate out-of-sample prediction accuracy (Fig. S64–S67†). The out-of-sample predictions are in excellent agreement with the observed $\Delta G^{\ddagger}_{OA}$.

Our initial attempts to incorporate aryl triflate electrophiles into this model using the aforementioned descriptor set were unsuccessful, leading to poor correlations and inaccurate predictions. We attribute this to C–X bond strength being an insufficient descriptor to differentiate between the reactivity of various leaving groups. Bond strength arguments, often using calculated BDEs, are used to rationalize relative oxidative addition reactivity for different substrates, such as for site selectivity in multihalogenated systems.[59–61] In our initial model (Fig. 2C and D), the IBSI term is essentially a step function: there are relatively narrow value distributions within the Ar–Br or Ar–Cl data sets, but a large gap between those data sets that reflects the weaker C–Br bond. Plotting a univariate correlation between $IBSI_{C-X}$ and $\Delta G^{\ddagger}_{OA}$ for all three electrophile classes reveals a similarly tiered structure (Fig. 2E). Strikingly, there is zero correlation between IBSI and $\Delta G^{\ddagger}_{OA}$, either within each electrophile class or across the entire data set. Furthermore, the relative ordering of bond strength (C–O > C–Cl > C–Br) is inconsistent with the fact that aryl triflates react faster than identically-substituted aryl bromides with $Pd(PCy_3)_2$ (k_{PhOTf}/k_{PhBr} ~100). Clearly, bond strength on its own is a poor predictor of oxidative addition reactivity when comparing two substrates with either the same[62] or different leaving groups.

To account for additional transition state stabilization by the leaving group itself, which builds up negative charge as the C–X bond is broken (Fig. 2A), we used a simple descriptor of anion stability: the pK_a of the leaving group's conjugate acid. Adding the pK_a values for HOTf, HBr, and HCl (−11.3, −4.4, and 0.2 respectively, previously measured in DCE as a non-polar solvent[63]) results in a unified predictive model (Fig. 2F). Both $IBSI_{C-X}$ and pK_a are required as descriptors, with the unified model re-weighting the IBSI term down by a factor of 2. Notably, the relative contributions of the ESP and *A*-value terms remain essentially constant.

This model provides, for the first time, a reliable method to quantitatively evaluate the relative reactivity of a hypothetical multisubstituted (hetero)aryl triflate, bromide, or chloride toward oxidative addition with a Pd(0) complex without the need to calculate transition state energies. We again performed cross-validation with a set of five random 60/40 training/test data partitions, which give excellent agreement between experimental and predicted values (Fig. S69–S73†). Of the 79 substrates, there are only four examples identified as prediction

Table 2 Linear regression coefficients and % contribution to predicted $\Delta G^{\ddagger}_{OA}$ for min/max scaled descriptors

Model	ESP_1	ESP_2	$(A_1 + A_2)$	IBSI	pK_a	Int
Fig. 2C	−48.36	20.97	7.037	19.25	—	30.28
	51%	22%	7%	20%	—	—
Fig. 2F	−51.65	23.68	6.924	19.14	21.81	16.94
	42%	19%	6%	16%	18%	—

outliers (standardized residual ≥2, Table 1). There are no obvious features of these outliers that would point to systematic prediction errors for a particular substructure; there are several similar examples (bromobenzenes, fluoropyridines, and pyrimidines) that are predicted accurately.

Finally, to examine the relative contribution of each descriptor to the predicted $\Delta G^{\ddagger}_{OA}$ of the two models (Fig. 2C and F), we applied a min/max scaling to the descriptor values prior to multivariate regression. The coefficients of the normalized models and their relative contributions are shown in Table 2. In both models, ESP_1 is the most consequential descriptor, followed by ESP_2 at roughly half the weighting. In contrast, steric effects account for <10% of the predicted $\Delta G^{\ddagger}_{OA}$. The C–X bond strength as reported by the IBSI descriptor is also a relatively small contributor (16–20%), consistent with the observation of its poor correlation to $\Delta G^{\ddagger}_{OA}$ when X remains constant (Fig. 2E). In fact, the pK_a of HX is just as consequential for predicting $\Delta G^{\ddagger}_{OA}$ as the IBSI in the model from Fig. 2F (X = Cl, Br, OTf).

Mechanistic aspects of oxidative addition linked to molecular descriptors.

The predictive power of this reactivity model is a direct result of its mechanistic foundation. ESP_1 is related to the electrophilicity of the carbon undergoing oxidative addition, reflecting the degree of partial positive charge in the π-complex intermediate and transition state: a larger positive ESP_1 leads to a smaller $\Delta G^{\ddagger}_{OA}$ and thus faster oxidative addition. In contrast, ESP_2 reflects the degree of negative charge on the adjacent atom (C or N), where a larger negative ESP_2 leads to a faster oxidative addition. Considered together, these ESP terms indicate that a more polarized C=C or C=N bond in the substrate leads to faster oxidative addition. It follows from this analysis that the ESP at Pd in the intermediate and/or transition state should also affect the oxidative addition rate, with a larger positive ESP_{Pd} correlating with faster oxidative addition. We have confirmed this by determining ESP_{Pd} for a set of 11 calculated π-complex intermediates and 6 transition states (Fig. S40–S56†). Remarkably, there is a linear correlation between ESP_{Pd} for the π-complexes and $\Delta G^{\ddagger}_{OA}$ (Fig. 3A and S57†), revealing the significant effect that substrate–catalyst bonding has on the electronic structure, and therefore reactivity, of Pd.

Analyzing how the substrate binds to the catalyst also sheds light on the observed equal weights of the steric *A*-values for R^1 and R^2 in affecting $\Delta G^{\ddagger}_{OA}$ for the 2-halopyridine substrate series. Larger substituents in these positions destabilize the π-complex intermediate and oxidative addition transition state through steric repulsion between the bound substrate and the ancillary phosphine ligands. Because the Pd center coordinates to the C=N bond, substituents adjacent to either C or N will occupy roughly equivalent positions with respect to the phosphines. Comparing the calculated structures of the π-complex intermediates for 2-chloropyridine to its 3- and 6-trifluoromethyl substituted analogues illustrates this feature of the substrate–catalyst interaction (Fig. 3B). Importantly, this mechanistic insight into equal steric effects for R^1 and R^2 flows directly from our quantitative reactivity model.

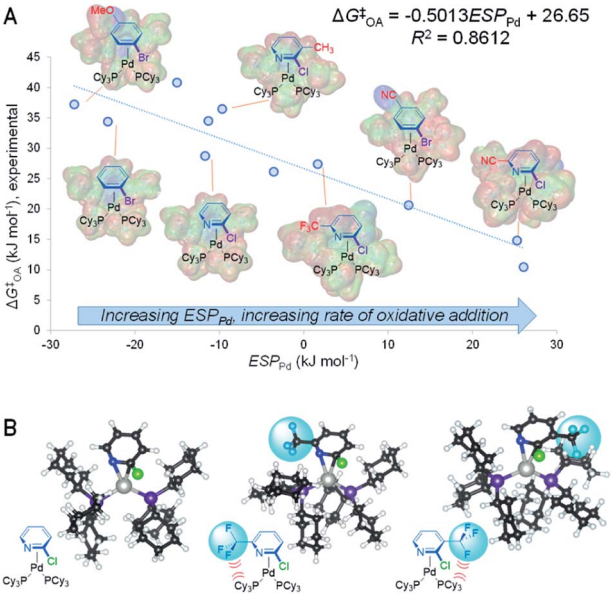

Fig. 3 Electronic and steric features of oxidative addition. (A) ESP_{Pd} for calculated π-complex intermediate structures correlates with oxidative addition rates; structures for 7 of 11 examples shown; electrostatic potential maps for each intermediate are overlaid onto the line structures. (B) Calculated structures of π-complex intermediates reveal how steric strain induced by R^1 and R^2 (here, $-CF_3$ groups) in 2-halopyridines affect oxidative addition reactivity in equal proportions.

Case study #1: predicting reaction rates

To test our hypothesis that the oxidative addition model is applicable to predicting outcomes for cross-coupling catalysis, we applied $\Delta G^{\ddagger}_{OA}$ predictions in three case studies. The first test case involves modeling the initial rates of Sonogashira coupling reactions, drawn from published data sets containing 410 individual rates (29 substrates and 17 catalysts, Fig. 4A).[64,65] We first predicted $\Delta G^{\ddagger}_{OA}$ for each of the 29 aryl bromides in the data sets, using the equation from Fig. 2C (the simpler model when considering only halide-based electrophiles); while 9 of these substrates are included in our experimental oxidative addition data set, the other 20 are out-of-sample predictions.

Remarkably, the predicted $\Delta G^{\ddagger}_{OA}$ values are linearly-correlated with the corresponding ln *k* values for all 17 investigated phosphine ligands (Fig. S74 and S75†). Correlations for three of these ligands – P(*n*Bu)$_3$, PCy$_3$, and P(*t*Bu)$_3$ – are shown in Fig. 4B. These correlations hold despite the fact that the Sonogashira reactions are conducted under different conditions

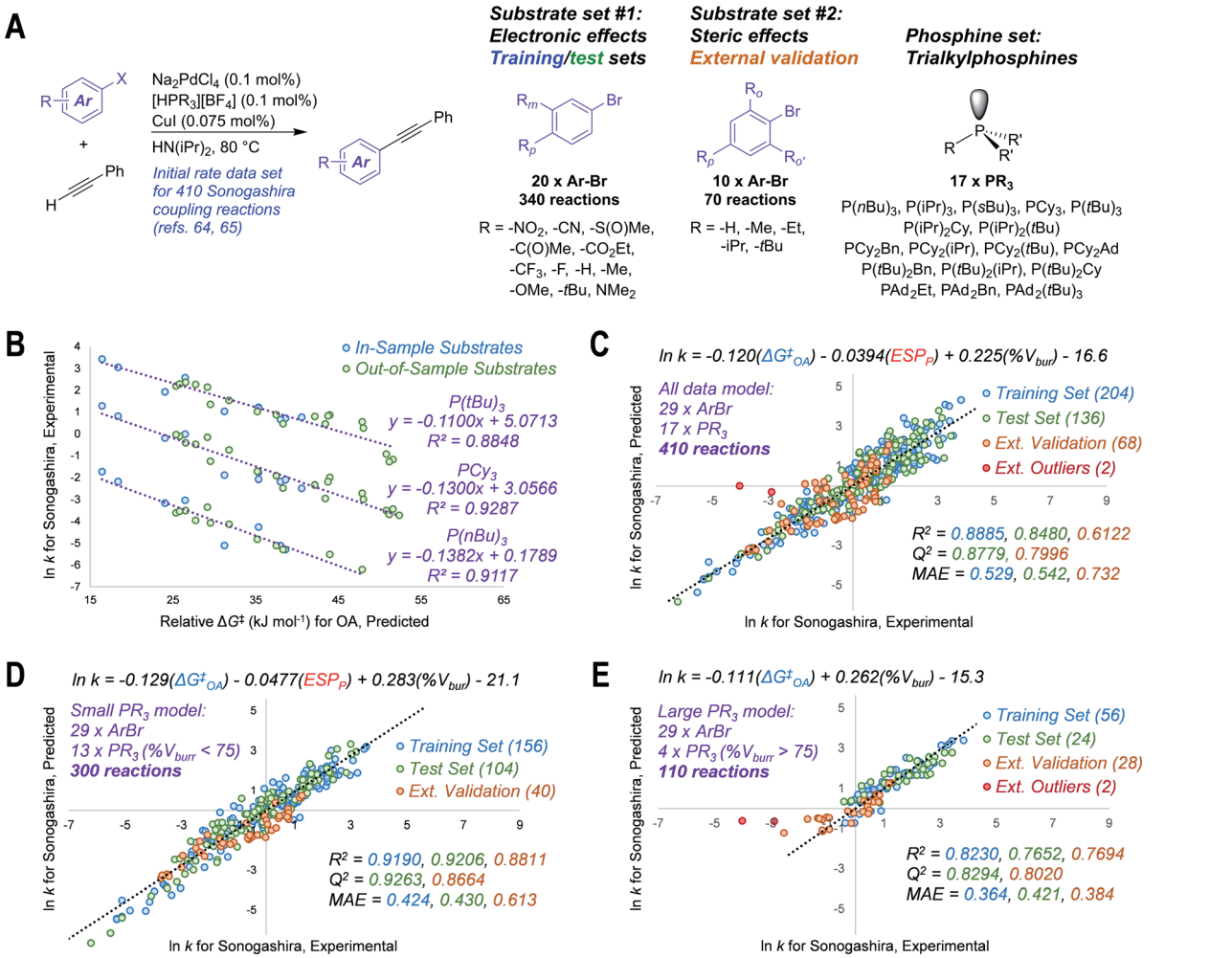

Fig. 4 Translating oxidative addition predictions to quantitative models of catalytic reactivity. (A) General reaction scheme and chemical space explored for 410 Sonogashira reactions, with two distinct substrate sets; initial rates determined previously.[64,65] (B) Univariate linear correlations between predicted $\Delta G^{\ddagger}_{OA}$ for oxidative addition to $Pd(PCy_3)_2$ and ln *k* for Sonogashira coupling with three phosphines; out-of-model substrates are Ar–Br molecules not included in $\Delta G^{\ddagger}_{OA}$ training set. (C) Unified three-descriptor model for predicting ln *k* for the entire set of 410 reactions (29 substrates, 17 ligands), with data partitioned into training (60% of set #1), test (40% of set #1), and external validation (set #2); two external outlier points (red) are not included in the external validation statistics. (D) Subset of the model with 13 "small" phosphines (% V_{bur} <75). (E) Subset of the model with 4 "large" phosphines (% V_{bur} >75); two external outlier points (red) are not included in the external validation statistics. MAE = mean absolute error. Colour-coding on R^2, Q^2, and MAE values corresponds to the matching data subset.

(higher temperature, different solvent) than our oxidative addition experiments, and the fact that our predicted $\Delta G^{\ddagger}_{OA}$ is derived from a model using only PCy_3. We suspect that this aspect of the model's usefulness stems from a consistency in the relative reactivity of the aryl halide substrates under different conditions, even if the absolute reaction rates differ. Thus, $\Delta G^{\ddagger}_{OA}$ can be applied to quantitatively predict the outcome of catalytic reactions for out-of-sample substrates, out-of-sample reaction conditions, and even out-of-sample catalysts.

We then expanded the application of $\Delta G^{\ddagger}_{OA}$ by combining it with descriptors for the 17 free phosphines to assemble a single and unified linear model to accurately predict ln *k* for the entire 410 Sonogashira reaction data set. Two descriptors were calculated for the free phosphines – the average ESP at phosphorus, and the percent buried volume (% V_{bur}) at phosphorus[66] – which were combined with $\Delta G^{\ddagger}_{OA}$ in a multivariate regression analysis. As shown in Fig. 4C, we obtain excellent linear fit and predictive power with initial rates spanning 10 orders of magnitude. These phosphine descriptors outperform the analogous descriptors calculated for the corresponding mono or bis(phosphine) Pd(0) complexes (Fig. S79 and S80†). The training and test sets used to build this model are from a random 60/40 split of substrate set #1, which focuses on electronic effects (Fig. 4A).

To challenge the model, we reserved substrate set #2, which focuses on steric effects, as an external validation set. Despite the fact that the Sonogashira rate prediction model training set (substrate set #1, blue and green points in Fig. 4C) contains no substrates with *ortho*-substituents, and therefore no information about steric effects on reaction rate, the model is still able to predict ln *k* for substrate set #2 with a mean absolute error of 0.732 (Q^2 = 0.7996). Only two reactions are identified as significant outliers: 2,4,6-triisopropylphenylbromide with

$P(tBu)_3$ and $PAd_2(tBu)$ (the most sterically-hindered substrate with the two largest ligands), which are much slower than the model predicts.

The ability to predict ln k for Sonogashira reactions of an out-of-sample substrate class stems directly from the generality of the predicted $\Delta G^{\ddagger}_{OA}$ from our oxidative addition reactivity model. The substrate molecular properties – electronics, sterics, and C–X bond strengths – are all encoded within the predicted $\Delta G^{\ddagger}_{OA}$ values by virtue of the structurally diverse oxidative addition training set. Thus, applying $\Delta G^{\ddagger}_{OA}$ as a single descriptor takes all of these molecular features into account, enabling accurate catalytic reactivity predictions even if the available training data is not as comprehensive.

Improved prediction accuracy can be achieved by separating the 410-member data set into two subsets based on phosphine ligand size. One set includes reactions using 13 phosphines with a % V_{bur} <75, and the other includes the 4 largest phosphines (% V_{bur} >75). For the small phosphine set, a slight reweighting of the three descriptors leads to smaller MAEs for training, test, and external data sets (Fig. 4D). For the large phosphines, we used a 70/30 training/test split due to the smaller number of data points. We also found that a simpler, two-descriptor model is superior for this subset, with only $\Delta G^{\ddagger}_{OA}$ and $\%V_{bur}$ needed to make accurate predictions (Fig. 4E). This partition into small and large phosphine sets is consistent with prior studies that describe a change in mechanism, where oxidative addition occurs from either bis(phosphine) or mono(phosphine) Pd(0) intermediates.[17,33,67] Notably, our predicted $\Delta G^{\ddagger}_{OA}$ is effective in both cases. This case study not only demonstrates how $\Delta G^{\ddagger}_{OA}$ can be used to predict how substitution patterns on the electrophile will affect the kinetic behavior of a coupling reaction, but also how $\Delta G^{\ddagger}_{OA}$ can be used in concert with catalyst-based descriptors to develop models that account for both substrate and catalyst effects on rate.

Case study #2: predicting site selectivity

The second case study tests the use of $\Delta G^{\ddagger}_{OA}$ in predicting site selectivity for cross-coupling when multiple reactive positions are present (Fig. 5). Previous approaches to this problem have involved spectroscopic descriptors,[68] the distortion–interaction transition state model,[62] and qualitative arguments based on empirical observations.[37,60] This latter method is most suitable for synthetic planning efforts, but it is largely applied "by analogy" to known systems, and it is not quantitative. Thus, formulating rapid but accurate predictions for the likely coupling site of structurally-complex multihalogenated substrates would be greatly beneficial for synthetic planning.

Because all of the descriptors in the $\Delta G^{\ddagger}_{OA}$ prediction model are local rather than global, one can calculate distinct $\Delta G^{\ddagger}_{OA}$ values for each reactive site in a molecule, with the predicted major site corresponding to the lowest $\Delta G^{\ddagger}_{OA}$. Assessing a series of multihalogenated heterocycles with reported experimental selectivities for Suzuki–Miyaura[60] and Buchwald–Hartwig[69–73] coupling reveals that these $\Delta G^{\ddagger}_{OA}$ predictions correctly identify the major site of reactivity across a diverse range of substrates, including many heterocycle classes (isoquinolines, diazines, and several 5-membered heterocycles) not included in our initial training set (Fig. 5). These predictions also correctly identify when a C–Cl position is more reactive than a C–Br

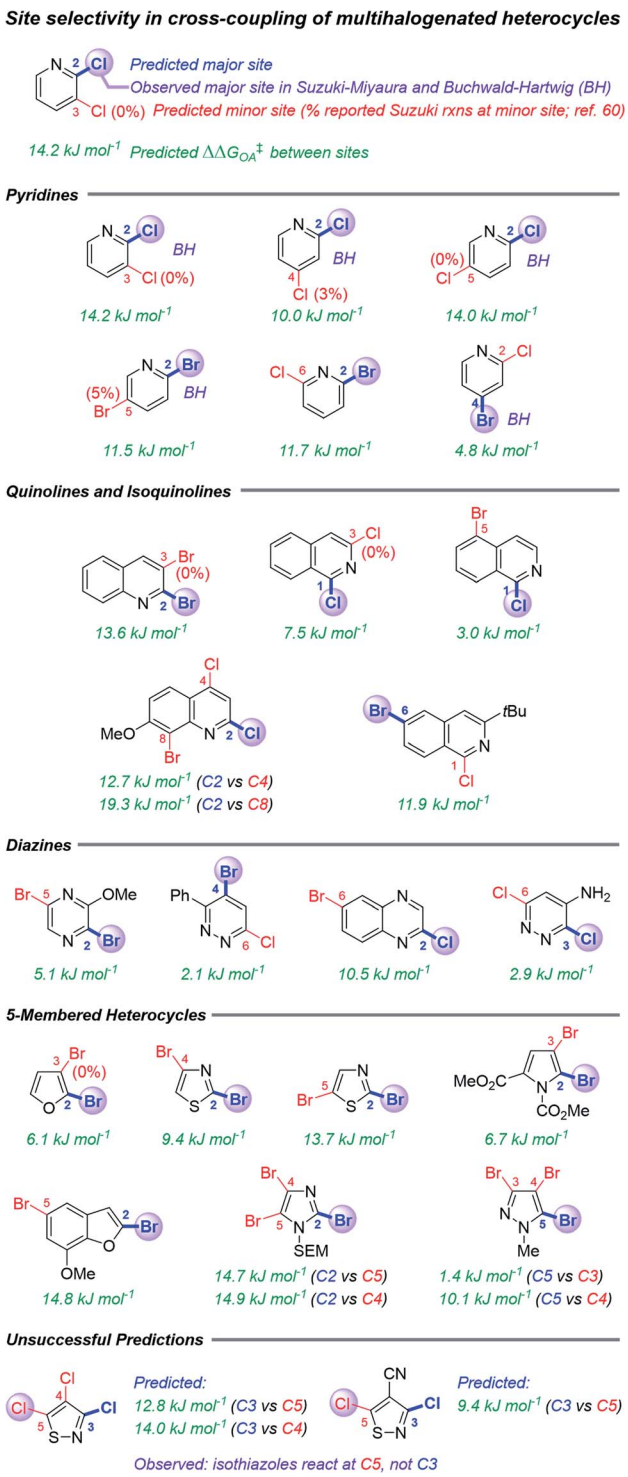

Fig. 5 Predicted and reported selectivities for multihalogenated heterocycles in Suzuki–Miyaura and Buchwald–Hartwig cross-coupling reactions (examples of Buchwald–Hartwig substrates denoted with "BH"). Coloured labels on the heterocycles correspond to predicted major site (blue), predicted minor site (red, along with percentage of exceptions as reported in ref. 60), and observed site (purple sphere). The magnitude of $\Delta\Delta G^{\ddagger}_{OA}$ between the two sites is given in green.

position in the same molecule, and *vice versa*. The model is, of course, not without limitations: predictions for two isothiazole substrates are not accurate, pointing to C3 as the preferred site over the correct C5 position.

In addition to identifying the major site of reactivity, the predictions are also quantitative (Fig. 6). A large difference between the $\Delta G^{\ddagger}_{OA}$ for each site ($\Delta\Delta G^{\ddagger}_{OA}$) indicates very high predicted selectivity for one site over another, while a small $\Delta\Delta G^{\ddagger}_{OA}$ indicates likely poor selectivity. Two specific examples of this are given in Fig. 6A. For Suzuki–Miyaura coupling of methyl 2,6-dichloronicotinate, our model predicts $\Delta\Delta G^{\ddagger}_{OA}$ = 5.4 kJ mol^{-1}, favoring C6 by ~7 : 1 at 65 °C. The observed selectivity using $Pd(PPh_3)_4$ as a catalyst at 65 °C is 5 : 1 C6 to C3 ($\Delta\Delta G^{\ddagger}$ = 4.5 kJ mol^{-1}).[74] For 3,6-dichloro-4-methoxypyridazine, our model predicts $\Delta\Delta G^{\ddagger}_{OA}$ = 0.7 kJ mol^{-1}, favoring C6 by ~1.3 : 1 at 100 °C (though this difference is smaller than the model MAE). The observed selectivity using $Pd(PPh_3)_4$ as a catalyst at 100 °C is 3 : 1 C6 to C3, ($\Delta\Delta G^{\ddagger}$ = 3.4 kJ mol^{-1}).[75] These predictions are also amenable to Buchwald–Hartwig coupling reactions: the predicted selectivity for 2,4-dichloropyridine is $\Delta\Delta G^{\ddagger}_{OA}$ = 10.0 kJ mol^{-1}, favoring C2 by 25 : 1 at 100 °C; a set of Buchwald–Hartwig aminations using a Xantphos-based catalyst proceed with C2 : C4 selectivity of 20 : 1 to 50 : 1 ($\Delta\Delta G^{\ddagger}$ = 9.3–12.1 kJ mol^{-1} at 100 °C).[73]

Site selectivity is known to be influenced by reaction conditions, such as catalyst and solvent.[37,60,76] Our prediction model is based on a simple monodentate phosphine using non-polar reaction solvents, which represents a standard combination used in synthetic applications. To illustrate how our model could guide the development of chemo/regiodivergent coupling reactions, we have applied predictions to substrates known to have tunable selectivity (Fig. 6B). First, 3,5-dichloropyridazine is predicted to have good selectivity for C3 over C5 ($\Delta\Delta G^{\ddagger}_{OA}$ = 10.6 kJ mol^{-1}), consistent with the observed selectivity using simple ligands (PPh_3, dppf); therefore, inverting this selectivity should require extensive catalyst/solvent screening. Researchers at Merck took this exact approach, discovering that the large QPhos ligand gives high C5 selectivity.[77]

Second, the predicted $\Delta\Delta G^{\ddagger}_{OA}$ for 2-chloro-5-bromopyridine is 0.2 kJ mol^{-1}, indicating effectively no selectivity; we confirmed this by oxidative addition of this substrate with $Pd(PCy_3)_2$, which gives a 1 : 1 mixture of C2 and C5 products. Thus, our prediction indicates achieving selectivity one way or the other will require more complex systems. Consistent with this, two previous studies reveal ligand-controlled reactivity at either C2 or C5, with high C2 selectivity requiring extensive screening and catalyst parameterization, and use of an unconventional diaminophosphine (dmapf).[69,78]

Finally, we predict that 2,4-dibromopyridine should be selective for C2 ($\Delta\Delta G^{\ddagger}_{OA}$ = 8.0 kJ mol^{-1}, C2 : C4 ~25 : 1 at 25 °C), which is exactly what is observed experimentally using homogeneous Pd catalysis.[79] A recent report revealed that heterogeneous, nanoparticle-based Pd catalysis is capable of inverting the selectivity to ~1 : 7 C2 : C4.[80] As for the examples above, overriding the predicted selectivity requires a dramatically different catalyst system.

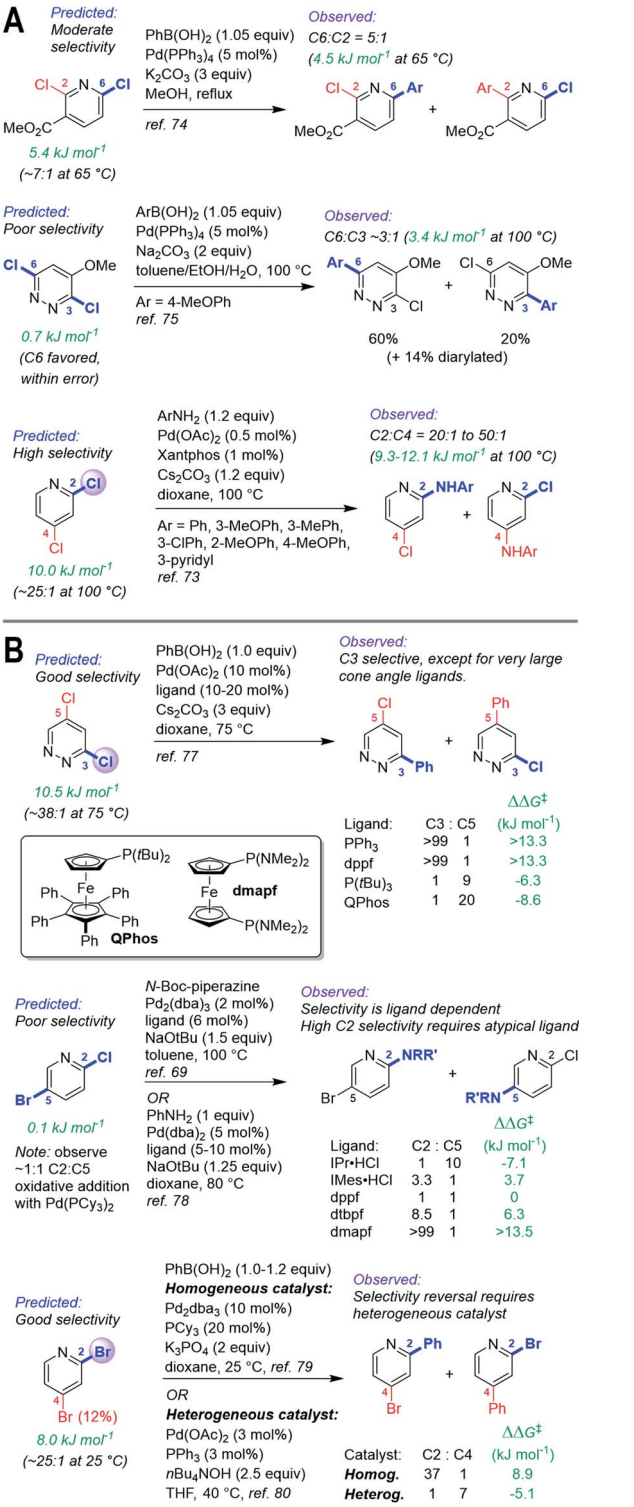

Fig. 6 (A) Quantitative selectivity predictions for dihalogenated heterocycles with small-to-medium $\Delta\Delta G^{\ddagger}_{OA}$ between two sites, and observed product ratios. (B) Predictions for substrates with observed tunable selectivity, demonstrating that "simple" catalysts are quantitatively consistent with predicted selectivities; overriding predicted reactivity requires targeted screening and/or catalyst design. Coloured labels on the heterocycles correspond to predicted major site (blue), predicted minor site (red, along with percentage of exceptions as reported in ref. 60), and observed site (purple sphere). The magnitude of $\Delta\Delta G^{\ddagger}_{OA}$ between the two sites is given in green.

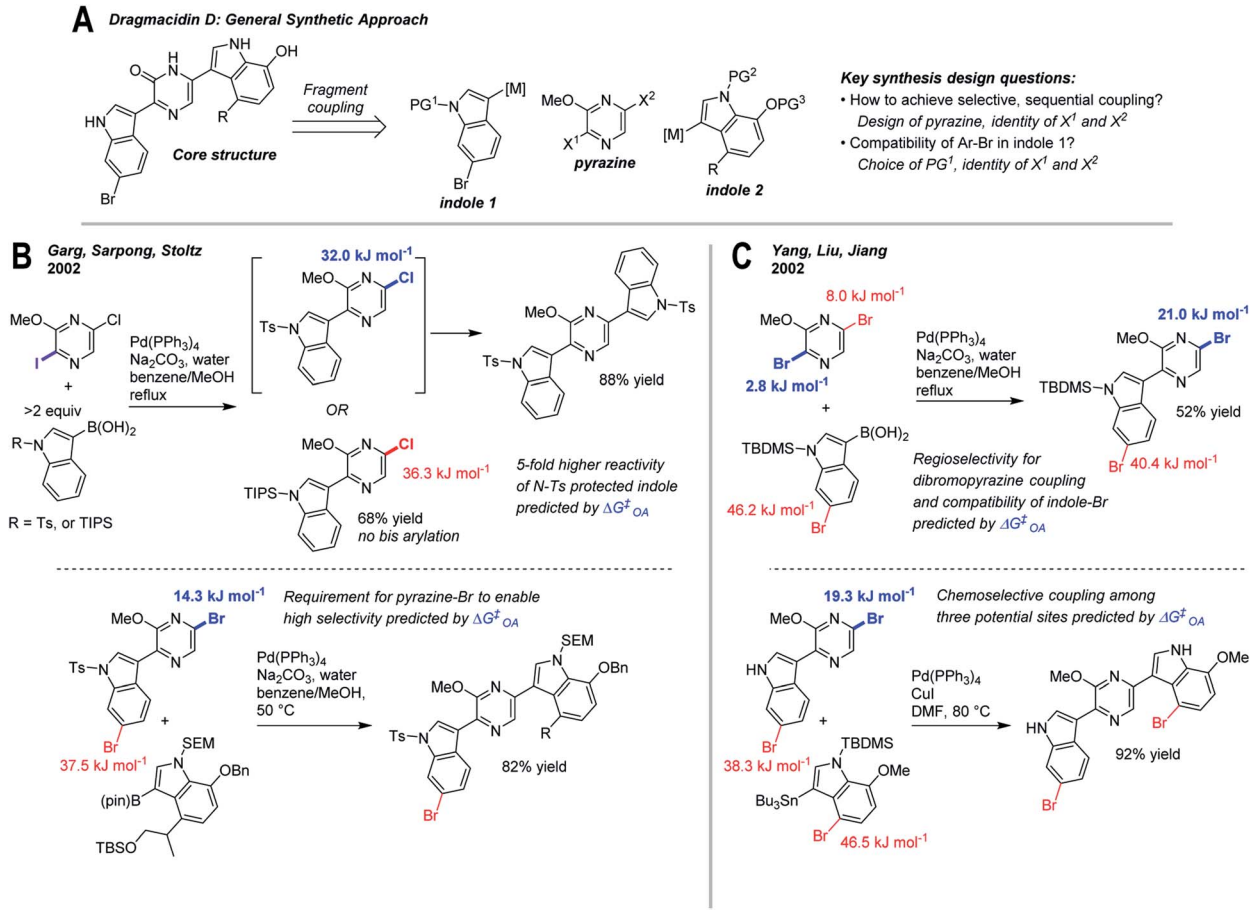

Fig. 7 Retrospective analysis of applying $\Delta G^{\ddagger}_{OA}$ predictions to synthesis design: dragmacidin D. (A) Retrosynthesis of core structure, involving selective fragment coupling to a dihalogenated pyrazine. (B) Approach involving differential halogenation, tosylate protecting group on indole 1, and switch from 5-chloro to 5-bromopyrazine intermediates for selective coupling.[81] (C) Approach involving regioselective coupling to dibromopyrazine, TBS protecting group on indole 1, and regioselective Stille coupling.[82]

Case study #3: retrospective synthesis planning

As a final case study, we have retrospectively applied $\Delta G^{\ddagger}_{OA}$ predictions to two reported synthesis toward dragmacidin D (Fig. 7).[81–83] The general sequence relies on two regioselective cross-coupling reactions to a dihalogenated pyrazine core (Fig. 7A). Among the key design questions are how to achieve selective, sequential couplings, and how to ensure compatibility with the existing Ar–Br in indole 1 (which is present in the natural product).[83]

Two approaches to this problem have been reported. En route to the first completed synthesis of dragmacidin D, Garg, Sarpong, and Stoltz (Fig. 7B)[81] conducted model studies using 2-iodo-5-chloro-3-methoxypyrazine to maximize site-selectivity, though they observed that the nature of the protecting group on the indole also has a significant effect on reactivity. With an *N*-Ts protecting group, bis(arylation) is readily achieved at elevated temperature, whereas with *N*-TIPS, the intermediate pyrazine is deactivated, preventing a second coupling. The remote electronic effect of the *N*-Ts group, which activates the C5 pyrazine position, is described as a fortuitous discovery. Applying our $\Delta G^{\ddagger}_{OA}$ predictions to these intermediates clearly reveals not only the existence but the magnitude of this effect, leading to ~5-fold higher predicted reactivity between *N*-Ts and *N*-TIPS substrates. Thus, a subtle but important reactivity difference could be anticipated based on predicted $\Delta G^{\ddagger}_{OA}$ prior to experimental work, and help guide protecting group selection.

The second coupling required a switch to the 2-iodo-5-bromo-3-methoxypyrazine to maximize site-selectivity, which again could be predicted based on our model. The $\Delta\Delta G^{\ddagger}_{OA}$ for the two Ar–Br positions in the pyrazine-indole intermediate used in the synthesis is 23.2 kJ mol^{-1}, consistent with the observed high selectivity. Hypothetical use of the corresponding 5-chloropyrazine intermediate gives a predicted $\Delta\Delta G^{\ddagger}_{OA}$ of <5 kJ mol^{-1} (~6 : 1 at 50 °C), which while still selective for the desired position, would likely lead to overreaction and yield loss. Again, this type of prediction could help to guide synthetic design and subsequent experimental investigations.

Yang, Liu, and Jiang reported a similar approach (Fig. 7C)[82] that employed 2,5-dibromo-3-methoxypyrazine as the pyrazine building block; a series of model studies established that

regioselective C2-coupling is possible. Despite the fact that both sites appear very similar, our model predicts that C2 is the major site, albeit with moderate selectivity ($\Delta\Delta G^{\ddagger}_{OA}$ = 5.1 kJ mol^{-1}, 6 : 1 at 80 °C); this lower selectivity may be reflected in the lower isolated yield relative to the differential halogenation strategy of Garg *et al.* In the subsequent Stille coupling, Yang *et al.* use the unprotected indole derivative, which we predict is ~10-fold less reactive than the corresponding *N*-Ts substrate; nevertheless, the desired reaction site is heavily favored relative to the other two Ar–Br positions, consistent with the observed regioselectivity.

Conclusions

We have demonstrated that a quantitative structure–reactivity model for oxidative addition, a key step in many catalytic mechanisms, enables accurate predictions for the outcome of various cross-coupling reactions. By correlating relative reaction rates with easily-obtained molecular descriptors, we can predict the reactivity of diverse (hetero)aryl electrophiles toward oxidative addition to Pd(0). This reactivity model links molecular structure to predicted $\Delta G^{\ddagger}_{OA}$ for any hypothetical substrate, with applicability well beyond the oxidative addition training set. We used these $\Delta G^{\ddagger}_{OA}$ values to predict rates and selectivities for many different catalytic reactions under various conditions, including Sonogashira, Suzuki, Buchwald–Hartwig, and Stille couplings.

Given the importance of palladium-catalyzed reactions in the synthesis of complex organic molecules, we anticipate that quantitative reactivity predictions could be used during synthetic planning to design substrates with high intrinsic selectivity, and/or to identify where achieving the desired selectivity is likely to be more challenging/resource intensive. Applying $\Delta G^{\ddagger}_{OA}$ predictions to hypothetical synthetic sequences and potential intermediates could therefore be used to design more selective routes and/or prioritize different potential routes prior to commencing experimental investigations. It could also be used to identify where extensive reaction development is necessary (*e.g.* overriding predicted selectivity), or where "simple" systems are likely to be successful. As we expand this oxidative addition reactivity model to incorporate additional sets of reaction conditions and catalysts, we expect it will not only shed new light on the mechanistic aspects of cross-coupling, but also find widespread use in refining and augmenting computer-aided synthesis design and automated reaction discovery/optimization. Finally, we are exploring quantitative reactivity models based on key steps in other catalytic mechanisms to generate accurate and general predictions across the synthesis landscape.

Data availability

Additional data files are available as part of the ESI,† including machine readable tables of descriptors (xlsx and csv formats) and coordinate files for calculated structures (xyz format).

Author contributions

J. Lu: conceptualization, methodology, investigation, validation, formal analysis, writing. S. Donnecke: investigation, formal analysis, writing. I. Paci: conceptualization, methodology, formal analysis, supervision, writing. D. C. Leitch: conceptualization, methodology, formal analysis, supervision, writing.

Conflicts of interest

There are no conflicts to declare.

Acknowledgements

We acknowledge with respect the Lekwungen peoples on whose traditional territory the University of Victoria (UVic) stands, and the Songhees, Esquimalt and WSÁNEĆ peoples whose historical relationships with the land continue to this day. We also acknowledge funding from the New Frontiers in Research Fund – Exploration (DCL) and NSERC Discovery Grant program (IP and DCL). Supercomputing resources at Westgrid and Compute Canada were integral to this work.

References

1 L.-C. Campeau and N. Hazari, *Organometallics*, 2019, **38**, 3–35.
2 J. Magano and J. R. Dunetz, *Chem. Rev.*, 2011, **111**, 2177–2250.
3 E. V. Vinogradova, C. Zhang, A. M. Spokoyny, B. L. Pentelute and S. L. Buchwald, *Nature*, 2015, **526**, 687–691.
4 K. Wang, A. Osuka and J. Song, *ACS Cent. Sci.*, 2020, **6**, 2159–2178.
5 P. S. Kutchukian, J. F. Dropinski, K. D. Dykstra, B. Li, D. A. DiRocco, E. C. Streckfuss, L.-C. Campeau, T. Cernak, P. Vachal, I. W. Davies, S. W. Krska and S. D. Dreher, *Chem. Sci.*, 2016, **7**, 2604–2613.
6 B. Mahjour, Y. Shen, W. Liu and T. Cernak, *Nature*, 2020, **580**, 71–75.
7 S. K. Kariofillis, S. Jiang, A. M. Żurański, S. S. Gandhi, J. I. M. Alvarado and A. G. Doyle, *J. Am. Chem. Soc.*, 2022, **144**, 1045–1055.
8 A. B. Santanilla, E. L. Regalado, T. Pereira, M. Shevlin, K. Bateman, L.-C. Campeau, J. Schneeweis, S. Berritt, Z.-C. Shi, P. Nantermet, Y. Liu, R. Helmy, C. J. Welch, P. Vachal, I. W. Davies, T. Cernak and S. D. Dreher, *Science*, 2015, **347**, 49–53.
9 M. Shevlin, *ACS Med. Chem. Lett.*, 2017, **8**, 601–607.
10 S. W. Krska, D. A. DiRocco, S. D. Dreher and M. Shevlin, *Acc. Chem. Res.*, 2017, **50**, 2976–2985.
11 S. M. Mennen, C. Alhambra, C. L. Allen, M. Barberis, S. Berritt, T. A. Brandt, A. D. Campbell, J. Castañón, A. H. Cherney, M. Christensen, D. B. Damon, J. Eugenio de Diego, S. García-Cerrada, P. García-Losada, R. Haro, J. Janey, D. C. Leitch, L. Li, F. Liu, P. C. Lobben, D. W. C. MacMillan, J. Magano, E. McInturff, S. Monfette,

R. J. Post, D. Schultz, B. J. Sitter, J. M. Stevens, I. I. Strambeanu, J. Twilton, K. Wang and M. A. Zajac, *Org. Process Res. Dev.*, 2019, **23**, 1213–1242.
12 C. L. Allen, D. C. Leitch, M. S. Anson and M. A. Zajac, *Nat. Catal.*, 2019, **2**, 2–4.
13 E. S. Isbrandt, R. J. Sullivan and S. G. Newman, *Angew. Chem., Int. Ed.*, 2019, **58**, 7180–7191.
14 B. Mahjour, Y. Shen and T. Cernak, *Acc. Chem. Res.*, 2021, **54**, 2337–2346.
15 N. Fey, A. C. Tsipis, S. E. Harris, J. N. Harvey, A. G. Orpen and R. A. Mansson, *Chem.-Eur.*, 2006, **12**, 291–302.
16 J. Jover, N. Fey, J. N. Harvey, G. C. Lloyd-Jones, A. G. Orpen, G. J. J. Owen-Smith, P. Murray, D. R. J. Hose, R. Osborne and M. Purdie, *Organometallics*, 2010, **29**, 6245–6258.
17 Z. L. Niemeyer, A. Milo, D. P. Hickey and M. S. Sigman, *Nat. Chem.*, 2016, **8**, 610–617.
18 K. Wu and A. G. Doyle, *Nat. Chem.*, 2017, **9**, 779–784.
19 D. J. Durand and N. Fey, *Chem. Rev.*, 2019, **119**, 6561–6594.
20 N. Fey, A. Koumi, A. V. Malkov, J. D. Moseley, B. N. Nguyen, S. N. G. Tyler and C. E. Willans, *Dalton Trans.*, 2020, **49**, 8169–8178.
21 L. C. Gallegos, G. Luchini, P. C. St. John, S. Kim and R. S. Paton, *Acc. Chem. Res.*, 2021, **54**, 827–836.
22 T. Gensch, G. d P. Gomes, P. Friederich, E. Peters, T. Gaudin, R. Pollice, K. Jorner, A. Nigam, M. L. D'Addario, M. S. Sigman and A. Aspuru-Guzik, *J. Am. Chem. Soc.*, 2022, **144**, 1205–1217.
23 A. W. McFord, C. P. Butts, N. Fey and R. W. Alder, *J. Am. Chem. Soc.*, 2021, **143**, 13573–13578.
24 D. J. Durand and N. Fey, *Acc. Chem. Res.*, 2021, **54**, 837–848.
25 B. Meyer, B. Sawatlon, S. Heinen, O. A. von Lilienfeld and C. Corminboeuf, *Chem. Sci.*, 2018, **9**, 7069–7077.
26 D. T. Ahneman, J. G. Estrada, S. Lin, S. D. Dreher and A. G. Doyle, *Science*, 2018, **360**, 186–190.
27 C. B. Santiago, J.-Y. Guo and M. S. Sigman, *Chem. Sci.*, 2018, **9**, 2398–2412.
28 B. Maryasin, P. Marquetand and N. Maulide, *Angew. Chem., Int. Ed.*, 2018, **57**, 6978–6980.
29 A. F. Zahrt, J. J. Henle, B. T. Rose, Y. Wang, W. T. Darrow and S. E. Denmark, *Science*, 2019, **363**, eaau5631.
30 T. Toyao, Z. Maeno, S. Takakusagi, T. Kamachi, I. Takigawa and K. Shimizu, *ACS Catal.*, 2020, **10**, 2260–2297.
31 F. Sandfort, F. Strieth-Kalthoff, M. Kühnemund, C. Beecks and F. Glorius, *Chem*, 2020, **6**, 1379–1390.
32 M. D. Wodrich, A. Fabrizio, B. Meyer and C. Corminboeuf, *Chem. Sci.*, 2020, **11**, 12070–12080.
33 S. H. Newman-Stonebraker, S. R. Smith, J. E. Borowski, E. Peters, T. Gensch, H. C. Johnson, M. S. Sigman and A. G. Doyle, *Science*, 2021, **374**, 301–308.
34 J. A. Hueffel, T. Sperger, I. Funes-Ardoiz, J. S. Ward, K. Rissanen and F. Schoenebeck, *Science*, 2021, **374**, 1134–1140.
35 Y. Shen, J. E. Borowski, M. A. Hardy, R. Sarpong, A. G. Doyle and T. Cernak, *Nat. Rev. Methods Primers*, 2021, **1**, 1–23.
36 J. A. Labinger, *Organometallics*, 2015, **34**, 4784–4795.
37 E. K. Reeves, E. D. Entz and S. R. Neufeldt, *Chem.-Eur.*, 2021, **27**, 6161–6177.
38 B. A. Anjali and C. H. Suresh, *ACS Omega*, 2017, **2**, 4196–4206.
39 C. Sandford, L. R. Fries, T. E. Ball, S. D. Minteer and M. S. Sigman, *J. Am. Chem. Soc.*, 2019, **141**, 18877–18889.
40 M. Kashihara, C. P. Gordon and C. Copéret, *Org. Lett.*, 2020, **22**, 8910–8915.
41 M. Busch, M. D. Wodrich and C. Corminboeuf, *ACS Catal.*, 2017, **7**, 5643–5653.
42 H. M. Senn and T. Ziegler, *Organometallics*, 2004, **23**, 2980–2988.
43 M. Ahlquist and P.-O. Norrby, *Organometallics*, 2007, **26**, 550–553.
44 C. L. McMullin, J. Jover, J. N. Harvey and N. Fey, *Dalton Trans.*, 2010, **39**, 10833–10836.
45 C. Amatore, A. Jutand, F. Khalil, M. A. M'Barki and L. Mottier, *Organometallics*, 1993, **12**, 3168–3178.
46 M. Portnoy and D. Milstein, *Organometallics*, 1993, **12**, 1665–1673.
47 F. Barrios-Landeros, B. P. Carrow and J. F. Hartwig, *J. Am. Chem. Soc.*, 2009, **131**, 8141–8154.
48 E. A. Mitchell, P. G. Jessop and M. C. Baird, *Organometallics*, 2009, **28**, 6732–6738.
49 B. U. W. Maes, S. Verbeeck, T. Verhelst, A. Ekomié, N. von Wolff, G. Lefèvre, E. A. Mitchell and A. Jutand, *Chem.-Eur.*, 2015, **21**, 7858–7865.
50 C. H. Suresh, P. Alexander, K. P. Vijayalakshmi, P. K. Sajith and S. R. Gadre, *Phys. Chem. Chem. Phys.*, 2008, **10**, 6492–6499.
51 F. B. Sayyed and C. H. Suresh, *New J. Chem.*, 2009, **33**, 2465–2471.
52 G. S. Remya and C. H. Suresh, *Phys. Chem. Chem. Phys.*, 2016, **18**, 20615–20626.
53 S. A. Grimmel and M. Reiher, *Faraday Discuss.*, 2019, **220**, 443–463.
54 S. R. Gadre, C. H. Suresh and N. Mohan, *Molecules*, 2021, **26**, 3289.
55 J. A. Hirsch, in *Topics in Stereochemistry*, John Wiley & Sons, Ltd, 1967, pp. 199–222.
56 J. Klein, H. Khartabil, J.-C. Boisson, J. Contreras-García, J.-P. Piquemal and E. Hénon, *J. Phys. Chem. A*, 2020, **124**, 1850–1860.
57 M. S. Sigman, K. C. Harper, E. N. Bess and A. Milo, *Acc. Chem. Res.*, 2016, **49**, 1292–1301.
58 V. Consonni, D. Ballabio and R. Todeschini, *J. Chem. Inf. Model.*, 2009, **49**, 1669–1678.
59 Y. Garcia, F. Schoenebeck, C. Y. Legault, C. A. Merlic and K. N. Houk, *J. Am. Chem. Soc.*, 2009, **131**, 6632–6639.
60 J. Almond-Thynne, D. C. Blakemore, D. C. Pryde and A. C. Spivey, *Chem. Sci.*, 2017, **8**, 40–62.
61 V. Palani, M. A. Perea and R. Sarpong, *Chem. Rev.*, 2022, DOI: 10.1021/acs.chemrev.1c00513.
62 C. Y. Legault, Y. Garcia, C. A. Merlic and K. N. Houk, *J. Am. Chem. Soc.*, 2007, **129**, 12664–12665.
63 E. Paenurk, K. Kaupmees, D. Himmel, A. Kütt, I. Kaljurand, I. A. Koppel, I. Krossing and I. Leito, *Chem. Sci.*, 2017, **8**, 6964–6973.

64 M. an der Heiden and H. Plenio, *Chem. Commun.*, 2007, 972–974.
65 M. R. an der Heiden, H. Plenio, S. Immel, E. Burello, G. Rothenberg and H. C. J. Hoefsloot, *Chem.-Eur.*, 2008, **14**, 2857–2866.
66 H. Clavier and S. P. Nolan, *Chem. Commun.*, 2010, **46**, 841–861.
67 F. Schoenebeck and K. N. Houk, *J. Am. Chem. Soc.*, 2010, **132**, 2496–2497.
68 S. T. Handy and Y. Zhang, *Chem. Commun.*, 2006, 299–301.
69 J. Ji, T. Li and W. H. Bunnelle, *Org. Lett.*, 2003, **5**, 4611–4614.
70 R. Jiang, D. Duckett, W. Chen, J. Habel, Y. Y. Ling, P. LoGrasso and T. M. Kamenecka, *Bioorg. Med. Chem. Lett.*, 2007, **17**, 6378–6382.
71 J. K. Laha, P. Petrou and G. D. Cuny, *J. Org. Chem.*, 2009, **74**, 3152–3155.
72 L. Qin, H. Cui, D. Zou, J. Li, Y. Wu, Z. Zhu and Y. Wu, *Tet. Lett.*, 2010, **51**, 4445–4448.
73 R. J. Burton, M. L. Crowther, N. J. Fazakerley, S. M. Fillery, B. M. Hayter, J. G. Kettle, C. A. McMillan, P. Perkins, P. Robins, P. M. Smith, E. J. Williams and G. L. Wrigley, *Tet. Lett.*, 2013, **54**, 6900–6904.
74 W. Yang, Y. Wang and J. R. Corte, *Org. Lett.*, 2003, **5**, 3131–3134.
75 E. Blaise, A. E. Kümmerle, H. Hammoud, J. X. de Araújo-Júnior, F. Bihel, J.-J. Bourguignon and M. Schmitt, *J. Org. Chem.*, 2014, **79**, 10311–10322.
76 E. K. Reeves, O. R. Bauman, G. B. Mitchem and S. R. Neufeldt, *Isr. J. Chem.*, 2020, **60**, 406–409.
77 X. Dai, Y. Chen, S. Garrell, H. Liu, L.-K. Zhang, A. Palani, G. Hughes and R. Nargund, *J. Org. Chem.*, 2013, **78**, 7758–7763.
78 M. H. Keylor, Z. L. Niemeyer, M. S. Sigman and K. L. Tan, *J. Am. Chem. Soc.*, 2017, **139**, 10613–10616.
79 C. Sicre, J.-L. Alonso-Gómez and M. M. Cid, *Tetrahedron*, 2006, **62**, 11063–11072.
80 N. W. J. Scott, M. J. Ford, N. Jeddi, A. Eyles, L. Simon, A. C. Whitwood, T. Tanner, C. E. Willans and I. J. S. Fairlamb, *J. Am. Chem. Soc.*, 2021, **143**, 9682–9693.
81 N. K. Garg, R. Sarpong and B. M. Stoltz, *J. Am. Chem. Soc.*, 2002, **124**, 13179–13184.
82 C.-G. Yang, G. Liu and B. Jiang, *J. Org. Chem.*, 2002, **67**, 9392–9396.
83 N. K. Garg and B. M. Stoltz, *Chem. Commun.*, 2006, 3769–3779.